Current Chemistry Letters 15 (2026) 387–396

Contents lists available at GrowingScience

Current Chemistry Letters

homepage: www.GrowingScience.com

Synthesis, characterization and study on the corrosion inhibition of E24 steel in acidic medium by 5,5'-(methylenebis(1,3,4-oxadiazole-5,2-diyl))bis(benzene-1,3-diamine): Approach combining chemistry and theoretical modeling

Assiya Atif[a*], Bendaoud Ahmed[b], Houssine Ait Sir[a], Salah Mohammed[b] and Zeroual abdellah[b]

[a]*Bioorganic Chemistry Team, Laboratory of Bioorganic Chemistry, Faculty of Sciences, Chouaib Doukkali University, 24000 El Jadida, Morocco*
[b]*Molecular Modeling and Spectroscopy Research Team, Faculty of Sciences, Chouaib Doukkali University, 24000 El Jadida, Morocco*

C H R O N I C L E

Article history:
Received June 2, 2025
Received in revised form
June 27, 2025
Accepted December 14, 2025
Available online
December 14, 2025

Keywords:
1,3,4-oxadiazole
Synthesis
Characterization
Monte Carlo
Non-Covalent Interactions

A B S T R A C T

This study presents the synthesis and characterization of the compound 5,5'-(methylenebis(1,3,4-oxadiazole-5,2-diyl))bis(benzene-1,3-diamine), by ^{1}H NMR, ^{13}C NMR and FTIR-ATR infrared spectroscopy and mass spectrometry. A theoretical study was carried out by a comprehensive and hierarchical methodology in order to evaluate the inhibitory behavior of the molecule 5,5'-(methylenebis(1,3,4-oxadiazole-5,2-diyl))bis(benzene-1,3-diamine) with respect to the corrosion of a Fe(110) type metal surface. Thus, examination of non-covalent interactions by NCI analysis. In addition, the study of adsorption on the metal surface was carried out by the Monte Carlo method.

© 2026 by the authors; licensee Growing Science, Canada.

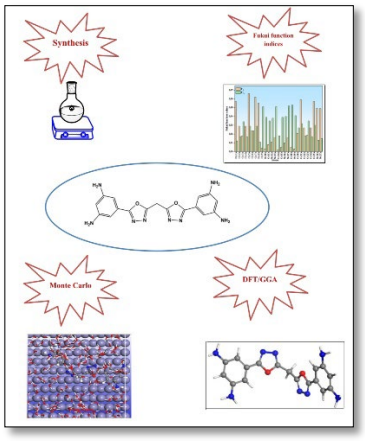

Graphical Representation

1. Introduction

Heterocyclic compounds are cyclic organic compounds that contain at least one heteroatom. Nitrogen, oxygen, and sulfur are the most commonly encountered heteroatoms.[1-5]

Heterocycles are a critically important class of compounds, accounting for more than half of all identified organic compounds. They are found in a multitude of drugs, including most vitamins, various natural products, biomolecules, and

* Corresponding author Tel.:
E-mail address assia.atif@gmail.com (A. Atif)
© 2026 by the authors; licensee Growing Science, Canada
doi: 10.5267/j.ccl.2025.12.007

biologically active compounds such as anticancer agents, antibiotics, anti-inflammatory drugs, antidepressants, antimalarial drugs, anti-HIV drugs, as well as their antimicrobial, antibacterial, antifungal, antiviral, and antidiabetic counterparts. They also include herbicides, fungicides, and insecticides. They often serve as the main structural component in synthesized pharmaceuticals and agrochemicals[6].

1,3,4-Oxadiazoles have been familiar heterocyclic compounds for nearly 90 years. This is primarily due to their widespread application in various sectors, including the pharmaceutical industry, where they are used as scintillating materials for drug synthesis, and in the dye industry. 1,3,4-Oxadiazole exhibits weak basicity due to the inductive influence of an additional heteroatom[7].

1,3,4-Oxadiazole derivatives are particularly notable. Compounds containing the 1,3,4-oxadiazole ring have their physicochemical and pharmacokinetic properties modified by its presence. Compared to other oxadiazole isomers, 1,3,4-oxadiazole derivatives display superior metabolic stability, increased water solubility, and lower lipophilicity. 1,3,4-Oxadiazole also serves as a bioisostere for compounds containing a carbonyl group such as esters, amides, and carbamates. The oxadiazole ring represents an essential component of the pharmacophore, having the ability to bind to the ligand. In certain situations, it acts as a flat aromatic linker to ensure the correct orientation of the molecule[8].

Several studies attest to the multidimensional effect of compounds containing the 1,3,4-oxadiazole ring in their composition. These derivatives have antibacterial[9], antimalarial[10], anti-inflammatory[11], antidepressant[12], anticancer[13], analgesic[14] and antiviral properties.[15,16]

Considering the richness of 1,3,4-oxadiazole domain, our study focuses on the synthesis and characterization of the compound 5,5'-(methylenebis(1,3,4-oxadiazole-5,2-diyl))bis(benzene-1,3-diamine) using ^{1}H NMR, ^{13}C NMR, FTIR-ATR infrared and mass spectrometry. Then, the evaluation of the inhibitory behavior of this molecule with respect to the corrosion of a Fe(110) type metal surface. In addition, the thermodynamic parameters and non-covalent interactions, an NCI (Non-Covalent Interaction) analysis were evaluated by adding a study of the adsorption on the metal surface.

2. Materials and Methods

2.1 Reagents and instruments

All reagents and solvents were obtained from Sigma Aldrich and used as received. Reaction progress is monitored by thin-layer chromatography (TLC) on aluminum sheets coated with Merck 60 F254 silica gel (thickness 0.2 nm). Revelation is carried out under a UV-Visible lamp (at 254 and 365 nm). The melting points of the synthesized compounds were determined using a Köfler bench and are not corrected to degrees Celsius. FTIR spectra were recorded on a SHIMADZU FT-IR 8400S spectrometer with a Smart iTR accessory and attenuated with total reflection crystal diamond (ATR) in the range (500-4000 cm^{-1}). Spectra were recorded on a Fourier transform JNM-ECZ500/S1 FT NMR SYSTEM (JEOL) (500 MHz for proton and 125 MHz for carbon 13) at the Centre National pour la Recherche Scientifique et Technique (CNRST) in Rabat. Spectra are referenced to the solvent in which they were made (^{1}H NMR: DMSO-d_6 = 2.5 ppm and ^{13}C NMR: DMSO-d_6 = 39.7 ppm). High-resolution mass spectrometry is performed on an Ultimate 3000-Exactive plus THERMO quadrupole-Orbitrap instrument, equipped with a collision cell from the Centre National pour la Recherche Scientifique et Technique (CNRST) in Rabat.

2.2 Synthesis

*2.2.1 Synthesis of diethyl malonate (**2**)*

Diethyl malonate **(2)** was synthesized by reacting (7 mmol) of malonic acid **(1)** with (15 ml) of ethanol, using a few drops of concentrated sulfuric acid as a catalyst. The mixture was refluxed for six hours. After stopping the reaction, the mixture was neutralized to pH 7 using 10% $NaHCO_3$ solution and then subjected to liquid-liquid extraction with chloroform. Following evaporation of the latter, diethyl malonate **(2)** was collected as a colorless liquid[17]. Yield: 86%, ^{1}H NMR(500MHz,DMSO-d_6,ppm): 1.30(t,J=10Hz,6H,$CH_{3(Ethyl)}$), 3.12(s,2H,CH_2), 4.29(q,J=10Hz,4H,$CH_{2(Ethyl)}$), ^{13}C NMR (125MHz,DMSO-d_6, ppm) : 168.22(2C=O), 68.99(CH_2), 44.90(2CH_2), 13.61(2CH_3), IR-ATR (cm^{-1}): 1715 υC=O, 1277 υC-H, MS(ESI): m/z = 161 $[M+H]^+$

2.2.2 Synthesis of malonohydrazide **(3)**

Condensation of 1 mmol of diethyl malonate **(2)** with 2 mmol of hydrated hydrazine under reflux for 2 hours at 50 °C gave us malonohydrazide **(3)** as a white solid[18]. Yield: 80%, m.p: 160 °C. ^{1}H NMR(500MHz,DMSO-d_6,ppm): 3.38(s,2H,CH_2), 4.82(s,4H,$NH_{2(Hydrazide)}$), 9.32(s,2H,$NH_{(Hydrazide)}$), ^{13}C NMR (125MHz,DMSO-d_6, ppm) : 162.32(2C=O), 46.03(CH_2), IR-ATR (cm^{-1}): 3362 υN-H, 3168-3215 υNH_2, 11630 υC=O, MS(ESI): m/z = 133 $[M+H]^+$

2.2.3. Synthesis of 5,5'-(methylenebis(1,3,4-oxadiazole-5,2-diyl))bis(benzene-1,3-diamine)

5,5'-(Methylenebis(1,3,4-oxadiazole-5,2-diyl))bis(benzene-1,3-diamine) **(5)** was prepared by reacting one equivalent of malonohydrazide **(3)** with two equivalents of a carboxylic acid derivative **(4)**, all in 15 ml of phosphoryl trichloride at reflux for 6 hours. Once cooled, the mixture was neutralized by adding 25% ammonia until the pH reached 7. The precipitate created was filtered and then recrystallized from ethanol **[19-21]**. Yield: 91%, m p: > 300 °C. ^{1}H NMR(500MHz,DMSO-

d_6,ppm): 3.69(s,2H,CH_2), 6.59(s,8H,NH_2), 7.61(s,2H,CHar), 7.87(s,4H,CHar), ^{13}C NMR (125MHz,DMSO-d_6, ppm) : 162.86(2C=N), 160.60(2C=N), 148.35(4Car), 127.30(2Car), 111.71(4Car), 104.51(2Car), 19.84(CH_2), IR-ATR (cm^{-1}): 3093-3156 υNH_2, 1650 υC=N, 1190 υC-O, MS(ESI): m/z = 365 $[M+H]^+$

3. Results and Discussion

3.1 Synthesis of 5,5'-(methylenebis(1,3,4-oxadiazole-5,2-diyl))bis(benzene-1,3-diamine)

Malonic acid **(1)** was esterified in ethanol using sulfuric acid as a catalyst for six hours at reflux. Following treatment of the reaction mixture, the diethyl malonate compound **(2)** was recovered at a rate of 86%[17]. Then, diethyl malonate **(2)** was reacted with two equivalents of hydrated hydrazine at 50 °C for two hours to form malonohydrazide **(3)**[18]. Finally, the preparation of 5,5'-(methylenebis(1,3,4-oxadiazole-5,2-diyl))bis(benzene-1,3-diamine) **(5)** resulted from the combination of malonohydrazide **(3)** with two equivalents of a carboxylic acid derivative **(4)** in the presence of phosphoryl trichloride[19-21].

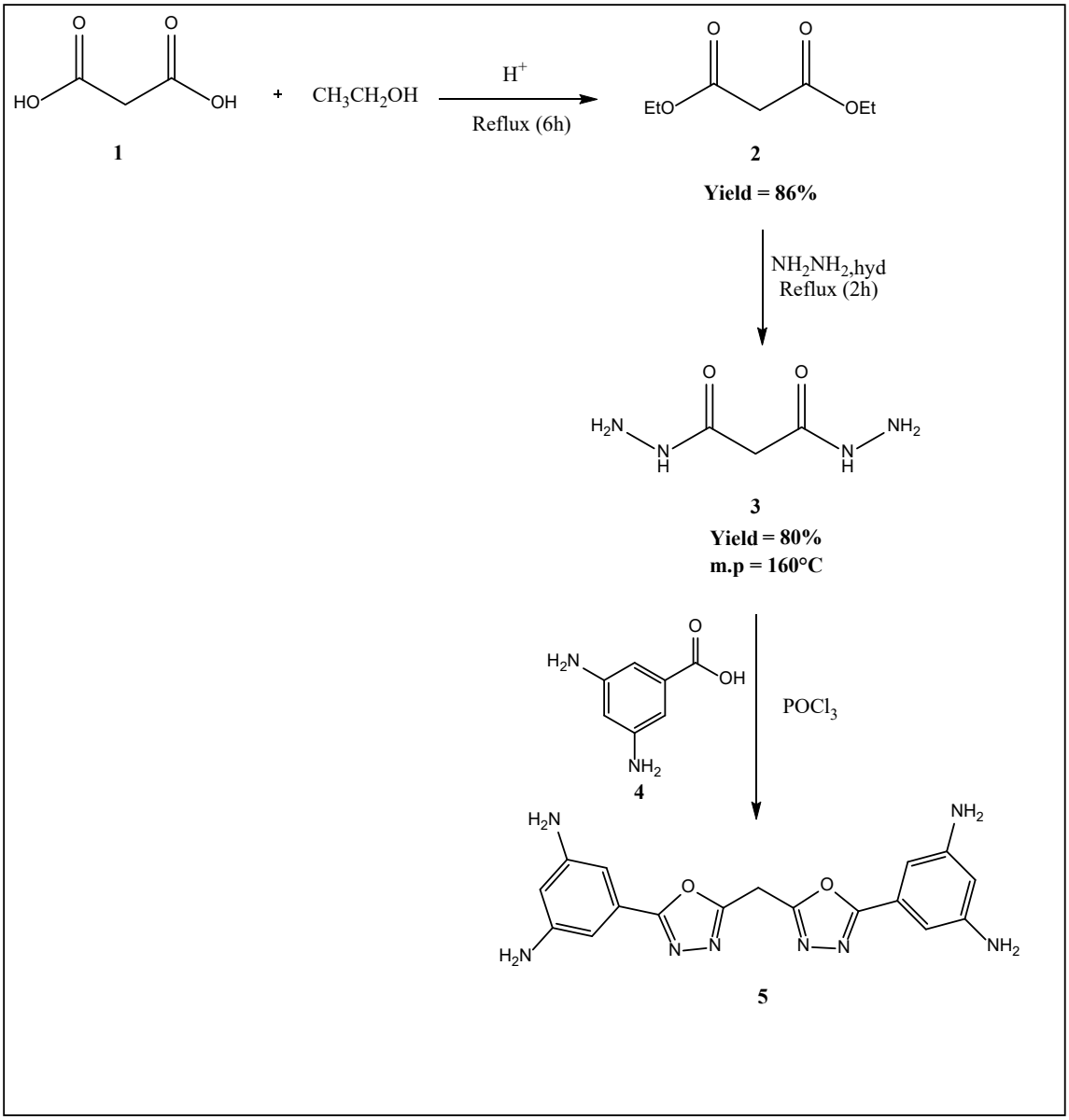

Scheme 1. Procedure for Synthesis of 5,5'-(methylenebis(1,3,4-oxadiazole-5,2-diyl))bis(benzene-1,3-diamine)

The structure of 5,5'-(methylenebis(1,3,4-oxadiazole-5,2-diyl))bis(benzene-1,3-diamine) **(5)** was confirmed by ^{1}H NMR, ^{13}C NMR, IR, and mass spectrometry.

Analysis of the ^{1}H NMR spectrum revealed a singlet at 3.69 ppm incorporating two CH_2 protons, as well as a signal at 6.59 ppm attributable to the amine proton and signals at 7.61 and 7.87 ppm corresponding to the aromatic protons. The ^{13}C NMR spectrum shows a signal at 19.84 ppm attributable to the CH_2 carbon, two signals at 162.86 and 160.60 ppm corresponding to the C=N bonds, and signals at 148.35, 127.30, 111.71 and 104.51 ppm due to the aromatic carbons. The

IR spectrum highlights a band at 3093-3156 cm^{-1} related to the NH_2 bond, a band at 1650 cm^{-1} corresponding to the C=N bond, and a band at 1190 cm^{-1} attributable to the C-O bond. The mass spectrum, taken in (ESI), shows a molecular peak related to the molecular ion m/z = 365$[M+H]^+$.

3.2 Theoretical calculations and simulations

3.2.1 Quantum chemical parameters and sigma profiles

In the framework of this theoretical study, an integrated and hierarchical methodology was applied to investigate the inhibitory efficiency of the molecule 5,5'-(methylene-bis(1,3,4-oxadiazole-5,2-diyl))bis(benzene-1,3-diamine) **(MOB)** against the corrosion of the Fe(110) metallic surface. The procedure was initiated by the geometric optimization of the molecule using the Dmol3[22] method implemented in Materials Studio[23]. The reactivity parameters were then determined by density functional theory (DFT) based on the frontier molecular orbitals HOMO and LUMO, allowing the calculation of the energy gap, electrophilicity and nucleophilicity indices, as well as Fukui functions, which are essential to identify the reactive sites of the molecule. In parallel, the molecular electrostatic potential (MEP) was computed at the DFT/6-311G(d,p) level using Gaussian09[24], providing a detailed mapping of electrophilic and nucleophilic regions favorable to electrostatic interactions with the metallic surface[25]. Thermodynamic properties, including Gibbs free energy, enthalpy, and entropy, were subsequently evaluated using the Dmol3 module, in order to assess the thermal stability of the inhibitor. The analysis of electron density and electrostatic potential profiles provided additional insights into the charge distribution within the molecule. Moreover, the Electron Localization Function (ELF)[26] was investigated using Python scripts to characterize the distribution of electron pairs and the nature of chemical bonding. Non-covalent interactions (NCI)[27] were further analyzed with Multiwfn[28] and visualized through VMD[29], highlighting the contribution of weak interactions such as hydrogen bonding, π–π stacking, and van der Waals forces. Finally, the adsorption of **MOB** on the Fe(110) surface was examined in two complementary steps. First, Monte Carlo simulations were carried out to determine the most stable adsorption configuration and to calculate the adsorption energies (total, rigid, and deformation). In the second step, molecular dynamics simulations were performed in Materials Studio[30] at two temperatures (298 K and 398 K) to evaluate the stability of the formed complex. The interaction and binding energies were calculated according to the following relations[31,32] :

$$E_{inter}=E_{mol/surface}-(E_{surface}+E_{mol}),\ E_{binding}=-E_{inter}$$

where $E_{mol/surface}$, and E_{mol} represent the total energies of the adsorbed system, the isolated surface, and the free molecule, respectively. The evolution of interatomic distances during the simulation was also monitored, providing additional information for the interpretation of the energetic results.

The evaluation of the inhibitory efficiency of the **MOB** compound against steel corrosion relies on an in-depth analysis of its electronic properties and molecular reactivity. Geometric optimization (A) reveals a well-organized structure, exhibiting highly electronegative sites, particularly around the nitrogen and oxygen atoms. These atoms carry significant negative partial charges, which suggests their ability to interact effectively with the metallic surface through electrostatic interactions or coordination bonds. The presence of such localized charges is often associated with a strong adsorption capability on metallic surfaces, thereby promoting the formation of a stable protective layer.

The analysis of the electronic distribution of frontier orbitals and Fukui functions provides important insights into the local reactivity of the studied molecule. The electronic density of the HOMO is mainly localized on the aromatic rings and around the nitrogen and oxygen heteroatoms. This indicates that these sites are the most favorable for electron donation toward the metallic surface of E-24 steel, thus promoting coordination-type interactions with the vacant orbitals of iron. In contrast, the LUMO exhibits a more extended distribution over other parts of the molecule, particularly on the substituted groups and heteroatoms, which reflects its capacity to accept electrons from the metal and contributes to the stabilization of adsorption through back-donation. With regard to Fukui indices, the f(–) function, which identifies regions prone to electrophilic attack, highlights high-density zones around nitrogen and oxygen atoms. These sites are therefore privileged centers for interaction with metallic cations, reinforcing adsorption via electron-donor interactions. Conversely, the f(+) function, associated with regions susceptible to nucleophilic attack, reveals localization on certain areas of the aromatic skeleton and on groups neighboring the heteroatoms. This suggests that the molecule can also receive electrons from the metallic surface, thereby contributing to chemisorption through a back-donation mechanism. The analysis of the Electron Localization Function (ELF) of the **MOB** inhibitor reveals a strong electronic density localized around oxygen and nitrogen atoms, with notable values such as V(O1) = 4.24 e, V(N3) = 2.94 e, V(N4) = 3 e, V(N5) = 2.97 e, and V(N6) = 3 e. These results reflect the presence of non-bonding electron pairs capable of coordinating with the vacant orbitals of iron, thereby favoring chemisorptive interactions between the molecule and the metallic surface. Moreover, the electronic delocalization observed within the aromatic rings suggests additional π–d type interactions with iron, strengthening the overall adsorption. The combination of these effects leads to the formation of a stable and compact protective film, which limits the penetration of corrosive species (H^+, Cl^-) and endows **MOB** with remarkable efficiency as a corrosion inhibitor for steel.

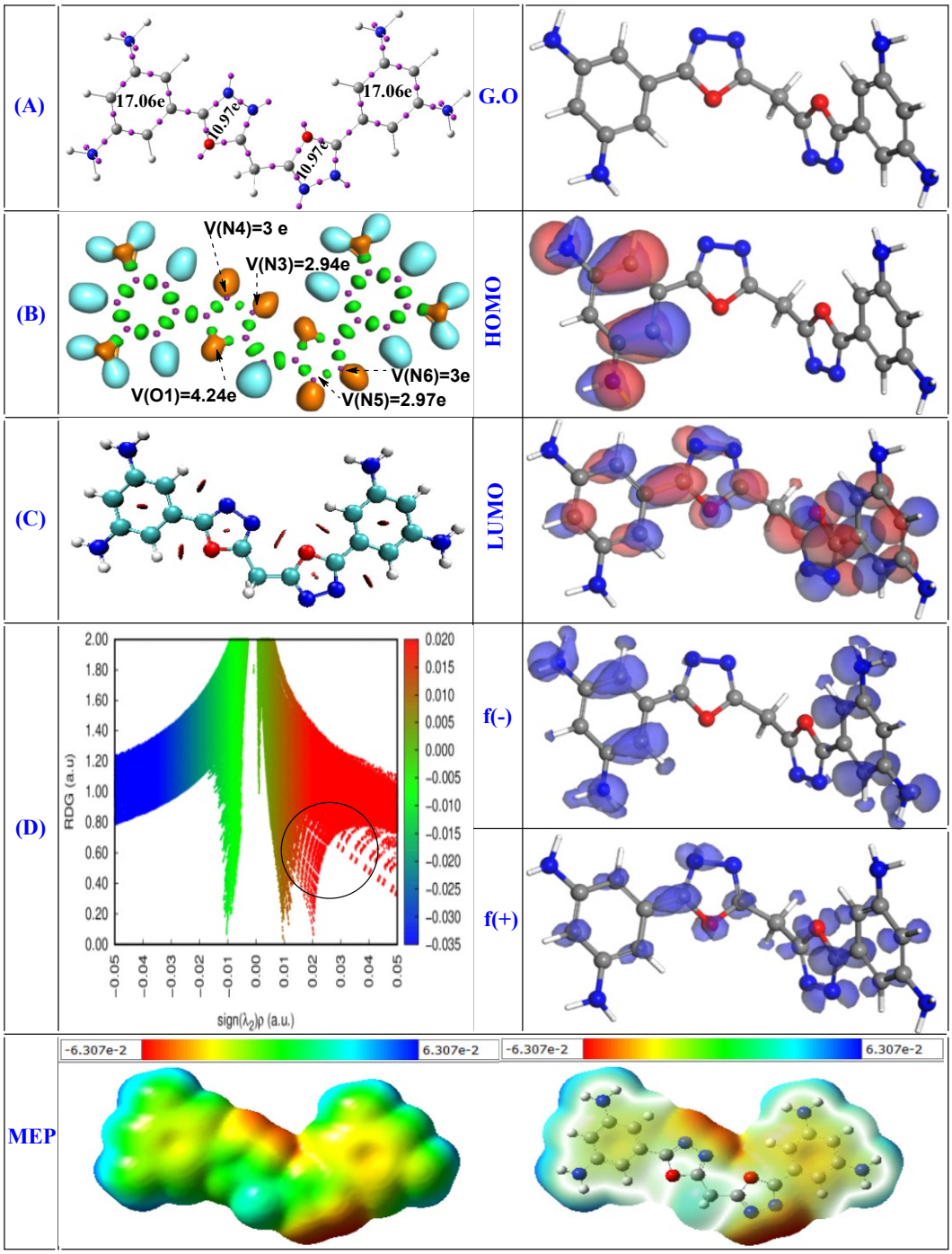

Fig. 1. (G.O) Optimized molecular structure, Highest occupied molecular orbital (HOMO), Lowest unoccupied molecular orbital (LUMO), (d) electrostatic potential (ESP) isosurface, (C,D) noncovalent interactions (NCI), (A,B) ELF positions basin attractors with ELF localization domains with the greatest relevance for valence basin populations are described at an ELF isosurface value of 0.80, molecular electrostatic potential (ESP), and (f(-), f(+)) Fukui function of **MOB** inhibitor, derived by using DFT/GGA calculations in the aqueous phase.

The analysis of non-covalent interactions (NCI) of the **MOB** inhibitor, illustrated by Figure (C) and the RDG graph (D), reveals the variety of stabilizing forces involved during adsorption on the metallic surface. The blue regions of the graph (negative values of sign(λ_2)ρ, $\approx$ –0.02 a.u.) indicate the presence of strong attractive interactions, mainly hydrogen bonds between the heteroatoms (N, O) of **MOB** and the atoms of the metallic surface, ensuring robust initial anchoring. The green regions (around sign(λ_2)$\rho \approx 0$) highlight van der Waals interactions, particularly distributed around the aromatic rings, playing a key role in the stabilization and alignment of **MOB** on the surface. As for the red regions (positive values of sign(λ_2)$\rho > 0.02$ a.u.), they represent steric repulsive interactions, which prevent excessive compaction and favor an optimal adjustment of the molecule on the metallic substrate. In addition to these contributions, a specific electronic interaction deserves to be emphasized: the π–d interactions between the aromatic rings of **MOB** and the d orbitals of iron. This type of interaction results from partial charge transfer between the delocalized π electrons of the aromatic rings and the vacant

orbitals of the metal, which reinforces chemisorptive adsorption in parallel with physisorptive adsorption. This π–d hybridization significantly contributes to the formation of a compact protective film, increasing the metal's resistance to the attack of corrosive agents (Cl^-, H^+). Thus, the combination of hydrogen bonding, van der Waals forces, regulatory steric interactions, and π–d contributions lead to the formation of a dense and stable inhibitory film. This film acts as an effective barrier, significantly reducing the diffusion of aggressive species toward the E-24 steel surface, thereby confirming the remarkable role of **MOB** as a corrosion inhibitor. The molecular electrostatic potential (MEP) map of the **MOB** inhibitor (Figure X) reveals negative regions (red/orange) localized around the O and N heteroatoms, which constitute active sites for adsorption onto the E-24 steel surface. The positive regions (blue), associated with hydrogen atoms, and intermediate zones (green/yellow) reflect secondary interactions. These features confirm that **MOB** can attach to the metallic surface both through coordination bonds involving heteroatoms and through π–d interactions of the aromatic rings. Altogether, these interactions lead to the formation of a stable protective film, effectively limiting the access of aggressive species (H^+, Cl^-) and thereby reducing corrosion.

Table 1. The HOMO and LUMO energy values together with the calculated other related parameters (in eV).

Inhibitor	E_{HOMO}	E_{LUMOH}	ΔE (eV)	η(eV)	σ (eV^{-1})	χ	ΔN	μ (Debye)
MOB	-0.18	-0.09	2.38	1.19	0.83	7.54	-1.62	5.2

The determination of the electronic parameters of the **MOB** inhibitor was carried out based on quantum chemical calculations using density functional theory (DFT), after molecular geometry optimization and evaluation of the frontier orbitals HOMO and LUMO. These values make it possible to deduce different reactivity descriptors, namely the energy gap (ΔE), hardness (η), softness (σ), electronegativity (χ), chemical potential (μ), and the number of transferred electrons (ΔN)[33]. These parameters are expressed as follows: energy gap (ΔE = ELUMO – EHOMO), chemical potential (μ = −(I + A)/2), electronegativity (χ = (I + A)/2), softness (σ = 1/η), and ΔN = (ΦFe – χinh) / [2 × (ηinh + ηFe)], where I and A represent the ionization potential and the electron affinity, calculated as I = −EHOMO and A = −ELUMO. (For metals, ηmetal ≈ 0 is often assumed, or values from the literature can be used; χFe is typically ≈ 4.8–5.0 eV)[34].

Table 2. Fukui function indices of **MOB** inhibitor, standard thermodynamic quantities of MOB molecules at 298.15 K, derived by using DFT/GGA calculations in the aqueous phase.

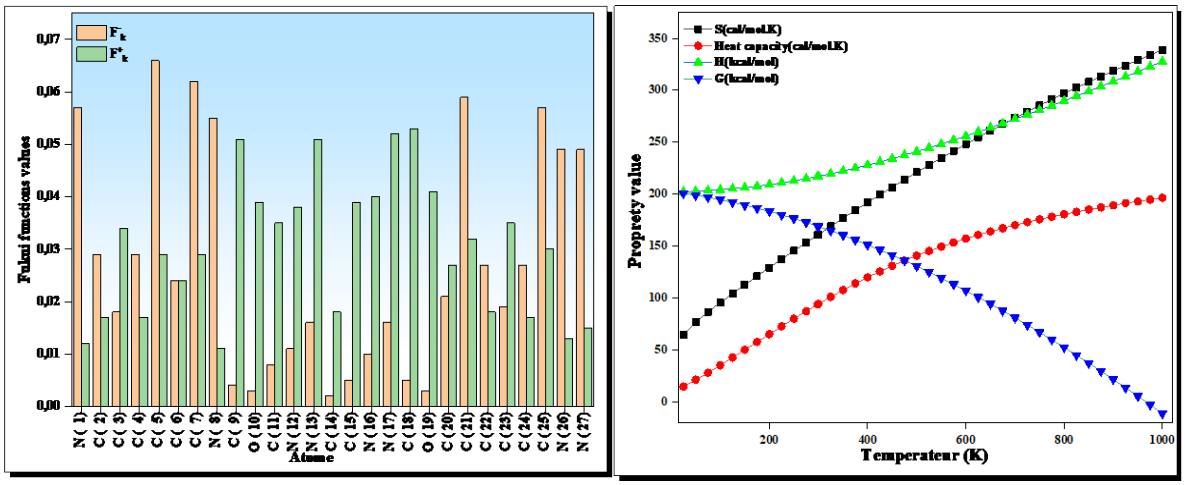

(A) **(B)**

The relatively high HOMO energy (−4.96 eV) indicates a significant ability of the molecule to donate electrons to the vacant orbitals of the metal, while the LUMO energy (−2.58 eV) points to the possibility of accepting electronic back-donation from the d orbitals of iron. Moreover, the small HOMO–LUMO gap (2.38 eV), combined with moderate hardness (1.19 eV) and relatively high softness (0.839 eV^{-1}), reflects enhanced reactivity and good polarizability, favoring the adsorption of the molecule onto the metallic surface. The calculated electronegativity of the inhibitor (≈3.77 eV), lower than that of iron (≈4.8 eV), suggests a net charge transfer from the inhibitor to the metal, thus confirming the electron-donor role of the molecule. Additionally, the relatively high dipole moment value (5.23 Debye) indicates a marked polar character, which facilitates the orientation and anchoring of the inhibitor on the Fe(110) surface. Altogether, these results highlight an interaction mechanism based on electron donation and back-donation, reflecting a mixed adsorption process of physisorption and chemisorption, leading to the formation of a stable protective layer capable of effectively reducing corrosion phenomena. In the framework of the local reactivity analysis of the **MOB** inhibitor, the Fukui functions f^+_k and f^-_k constitute reliable indicators for identifying the most reactive atomic sites toward nucleophilic and electrophilic attacks. The results show that atoms C(6), C(7), C(20), C(25), and C(26) display relatively high f^-_k values, reflecting their strong ability to undergo interactions with electrophilic species. In contrast, atoms C(8), C(15), C(16), C(18), and C(19) are

distinguished by high f^{+}_{k} values, indicating that they are the main sites likely to be attacked by nucleophilic agents. Moreover, the contribution of heteroatoms, particularly N(1) and O(12), highlights their role in complexation and adsorption onto the metallic surface. Thus, the differentiated distribution of Fukui indices reveals that the **MOB** inhibitor possesses multiple reactive centers capable of effectively interacting with E-24 steel, thereby favoring the establishment of stable chemical bonds and optimal surface coverage. This multifaceted reactivity confirms the inhibitory potential of the molecule by ensuring better protection against corrosion phenomena.

Within the framework of the thermodynamic study of the **MOB** inhibitor, the variations of enthalpy (H), entropy (S), heat capacity (Cp), and Gibbs free energy (G) as a function of temperature provide essential insights into the stability and feasibility of the processes involved. The results show that enthalpy (H) increases almost linearly with temperature, reflecting the growing absorption of thermal energy by the system. Similarly, entropy (S) rises significantly with temperature, indicating greater disorder and enhanced molecular motion at higher temperatures. Heat capacity (Cp) exhibits a rapid increase at low temperatures before tending toward a limiting value at higher temperatures, which reflects the progressive saturation of the vibrational degrees of freedom of the molecule. Conversely, Gibbs free energy (G) decreases continuously with increasing temperature, which indicates greater spontaneity of the processes at higher temperatures. Overall, these results suggest that the MOB inhibitor is thermodynamically stable and that its interactions become more favorable with rising temperature, thereby enhancing its potential efficiency under corrosion conditions on E-24 steel.

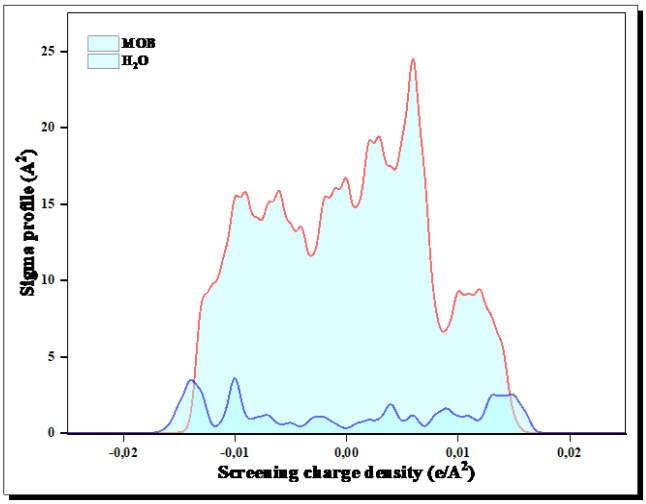

Fig. 2. Illustration of sigma profiles calculated using the DFT/GGA approach

The analysis of the charge density profile highlights the distribution of surface charges of the **MOB** inhibitor and makes it possible to evaluate its solvation behavior in the aqueous medium. The curve shows that the **MOB** inhibitor exhibits a much broader and more intense charge density distribution than that of the water molecule, with pronounced peaks in both positive and negative regions. This asymmetry reflects the presence of polarized zones within the molecule, promoting both electrostatic interactions and donor/acceptor-type bonding with the metallic surface. In comparison, the profile of water remains relatively weak and narrow, indicating a lower polarization capacity and more limited interactions. The strong intensity of the **MOB** profile suggests a greater ability to adsorb onto the E-24 steel surface, in competition with water molecules. This confirms that the inhibitor can effectively replace solvent molecules at the metal/solution interface, thereby ensuring denser protective coverage and enhanced inhibition of the corrosion process.

3.2.2 Molecular dynamic simulations (MDs)

In this study, a combined approach using Monte Carlo (MC) simulations and molecular dynamics (MD)[35] was applied with the Materials Studio software to examine the adsorption behavior of the inhibitor on the metallic surface. First, the Monte Carlo method was employed to explore the possible adsorption configurations of the molecule on the iron surface and to identify the energetically most favorable sites. At this stage, a simulation box was constructed by inserting a 20 Å vacuum above the metallic surface, which eliminates unwanted periodic interactions in the perpendicular direction and reproduces an environment close to the metal–solution interface. The upper part of the cell was then filled with the inhibitor molecule, as well as solvent molecules (H_2O) and HCl ions, to more accurately simulate the acidic corrosive medium. This protocol allows the evaluation not only of the inhibitor adsorption on the Fe(110) surface but also of the competitive effects of solvent molecules and aggressive ions. Next, the configurations obtained by MC were refined using molecular dynamics calculations to study the stability and temporal evolution of the interactions. The MD simulations were performed in the canonical ensemble (NVT)[36] at a temperature of 373 K, controlled by the Andersen thermostat. The time step was set to 1.0 fs for a total of 50,000 steps, corresponding to an effective duration of 50 ps. The initial velocities of the atoms were randomly assigned to ensure statistically representative sampling. The COMPASSIII[37] force field was used with automatic assignment of partial charges, enabling an accurate description of interatomic interactions for the entire system. This

combined MC–MD approach thus allows the identification of preferential adsorption sites of the inhibitor, the evaluation of competitive contributions from water and HCl ions, and the assessment of the stability of the protective layer formed on the metallic surface under conditions close to the actual corrosion environment.

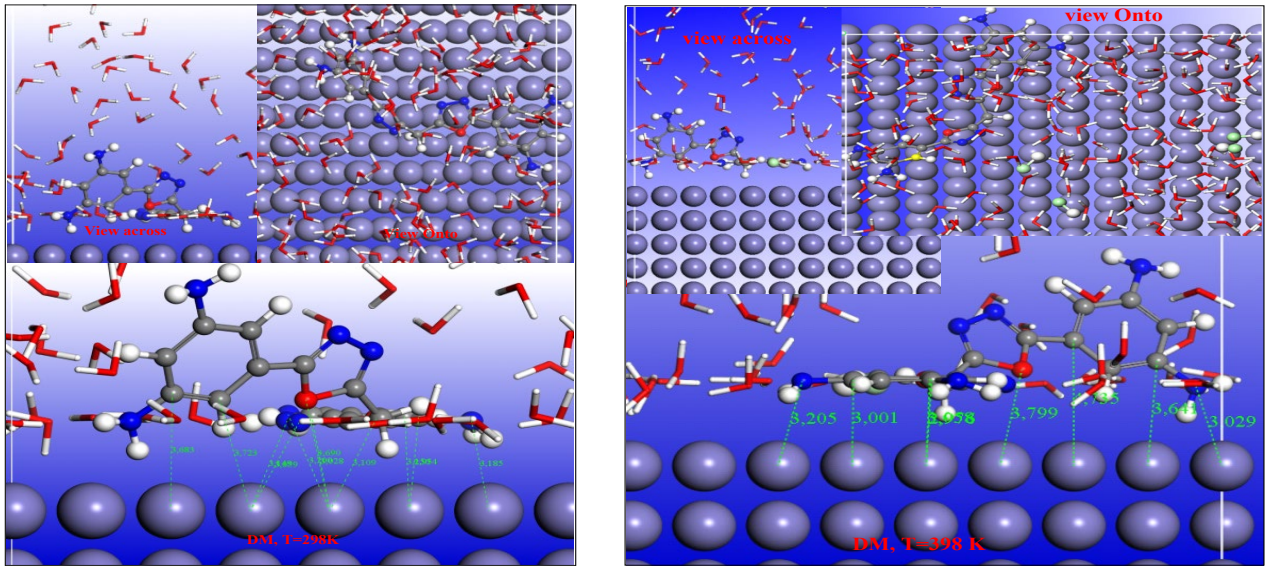

Fig. 3. Comparative Adsorption Behavior of an Organic Inhibitor on Fe(110) Surface at 298 K and 398 K: Molecular Dynamics Simulations.

Table 2. Monte Carlo simulation results.

Structures	Total energy	Adsorption energy	Rigid adsorption energy	Deformation energy	MOB : dEad/dNi	H2O : dEad/dNi	HCl : dEad/dNi
Fe (1 1 0)	-3.47E+03	-3.80E+03	-3.70E+03	-106.01	-239.31	-12.22	-14.08

Table 3. Molecular Dynamic results.

T(K)	**398**	**298**
$E_{complixe}$ (Kcal/mol)	-68424.00	-68218.70
E_{MOB} (Kcal/mol)	-67622.87	-67622.87
$E_{MOB + H2O+HCl}$ (Kcal/mol)	127.33	127.33
$E_{interaction}$ (Kcal/mol)	-928.46	-723.16
$E_{binding}$ (Kcal/mol)	928.46	723.16

The results from the Monte Carlo simulations (**Table 2**) and molecular dynamics simulations (**Table 3**), combined with structural visualizations at 298 K and 398 K, allow a detailed characterization of the interaction between the **MOB** inhibitor and the Fe(110) metallic surface. The adsorption energy obtained from Monte Carlo simulations is highly negative (−3800 kcal/mol), indicating a thermodynamically favorable interaction. The strongly negative value of dEad/dNi for **MOB** (−239.31) shows that this inhibitor is the main contributor to adsorption on the metallic surface, well above water (−12.22) and HCl (−14.08). Moreover, the moderate deformation energy (−106.02 kcal/mol) reflects a conformational adjustment of MOB to optimize its anchoring points on the surface. This adsorption is further confirmed and analyzed in detail by molecular dynamics at temperatures of 298 K and 398 K. At 298 K (**Fig. 1**), **MOB** adopts a planar orientation relative to the iron surface, with interatomic distances ranging from 3.028 Å to 4.109 Å. These distances indicate the presence of stable non-covalent interactions, typical of physisorption reinforced by π–d interactions with the surface orbitals of iron. This planar configuration maximizes surface coverage, favoring the formation of a homogeneous protective film. The interaction energy at this temperature is −723.17 kcal/mol, confirming the stability of the formed complex. The corresponding binding energy (723.17 kcal/mol) reflects effective attachment of the inhibitor to the metallic surface. At 398 K (**Fig. 2**), despite increased thermal motion, **MOB** maintains strong interaction with the surface, as evidenced by slightly modified but still favorable interatomic distances (3.001 Å to 3.799 Å). The orientation of **MOB** remains largely parallel, with a slight twist indicating additional conformational adjustment at the higher temperature. This molecular reorganization is corroborated by a more negative interaction energy (−928.46 kcal/mol) and a higher binding energy (928.46 kcal/mol) than those observed at 298 K, reflecting strengthened interactions and enhanced stability of the complex at elevated temperatures. These results highlight **MOB**'s ability to maintain, or even improve, its inhibitory performance under corrosive conditions, even at high temperatures, which is a significant advantage for industrial applications in harsh environments. Thus, the consistency between the observed distances (indicating effective interactions), adsorption energies, interaction energies, and binding energies confirms the high potential of **MOB** as a corrosion inhibitor, both at ambient temperature and under more aggressive thermal conditions.

4. Conclusion

This study confirms the structure of a novel 1,3,4-oxadiazole derivative, 5,5'-(methylenebis(1,3,4-oxadiazole-5,2-diyl))bis(benzene-1,3-diamine), by ^{1}H NMR, ^{13}C NMR, FTIR-ATR infrared spectroscopy and mass spectrometry. The evaluation of the inhibitory efficacy showed that 5,5'-(methylenebis(1,3,4-oxadiazole-5,2-diyl))bis(benzene-1,3-diamine) has a good adsorption capacity on metal surfaces, promoting the formation of a stable protective layer. Furthermore, the relatively high value of the dipole moment (5.23 Debye) reflects a marked polar character, which indicates a mixed adsorption of physisorption and chemisorption type, leading to the formation of a stable protective layer capable of effectively limiting corrosion phenomena and also thermodynamically stable. Its interactions become more favorable with increasing temperature, thus promoting its potential effectiveness in corrosion conditions on E24 steel. The Monte Carlo study shows the ability of 5,5'-(methylenebis(1,3,4-oxadiazole-5,2-diyl))bis(benzene-1,3-diamine) to maintain, or even improve, its inhibitory performance in corrosive environments even at high temperatures, which is a considerable asset for industrial applications in severe conditions. Thus, the consistency between the observed distances (indicating effective interactions), the adsorption, interaction and binding energies, confirms the high potential of the molecule as a corrosion inhibitor, both at room temperature and in more aggressive thermal conditions.

Funding

The authors declare that no funds, grants, or other support were received during the preparation of this manuscript.

Acknowledgements

The authors are grateful to for the research assistance from Bioorganic Chemistry Team, Faculty of Sciences, Chouaib Doukkali University, B.P. 20, 24000 El Jadida, Morocco and Molecular Modeling and Spectroscopy Research Team, Faculty of Science, ChouaibDoukkali University, P.O. Box 20, 24000 El Jadida, Morocco.

References

1. Kacka-Zych A. (**2025**) Synthesis of heterocycles via cycloaddition reactions with the participation of cyano-substituted nitroalkenes. Chem. Heterocycl. Compd., 61 (7/8) 317-319.
2. Jasiński R. (**2025**) Recent progress in the synthesis of nitropyrazoles and their hydrogenated analogs via noncatalyzed (3+ 2) cycloaddition reactions of conjugated nitroalkenes. Chem. Heterocycl. Compd., 61 (7/8) 286-289
3. Janowski, M., Demchuk, O. M., & Wujec, M. (**2025**). Antibacterial efficiency of compounds bearing 1, 2, 3-triazole scaffold: a critical review. Chem. Heterocycl. Compd., 61 (7/8) 290-302
4. Atif A., and Ait Sir H. (**2025**) Synthetic Approaches for Oxazole Derivatives: A Review. J. Heterocycl. Chem., 62 (11) 1808-1833
5. Al-Mulla, A. (**2017**) A review: biological importance of heterocyclic compounds. DPC., 9 (13) 141-147.
6. Eftekhari-Sis B., Zirak M., and Akbari A. (**2013**) Arylglyoxals in synthesis of heterocyclic compounds. Chem. Rev., 113 (5) 2958-3043.
7. Salahuddin Mazumder A., Yar M. S., Mazumder R., Chakraborthy G. S., Ahsan M. J., and Rahman M. U. (**2017**) Updates on synthesis and biological activities of 1, 3, 4-oxadiazole: A review. Synth. Commun., 47 (20) 1805-1847.
8. Kamboj S. (2010) HETEROCYCLIC 1, 3, 4-OXADIAZOLE COMPOUNDS WITH DIVERSE BIOLOGICAL ACTIVITIES-A COMPREHENSIVE REVIEW. J. Pharm. Res., 3 (12) 2993-2997.
9. Wang L., Zhou X., Lu H., Mu X., and Jin L. (**2020**) Synthesis and antibacterial evaluation of novel 1, 3, 4-Oxadiazole derivatives containing sulfonate/carboxylate moiety. mol., 25 (7) 1488-1502.
10. Khalilullah H., J Ahsan M., Hedaitullah M., Khan S., and Ahmed B. (**2012**) 1, 3, 4-oxadiazole: a biologically active scaffold. Mini-Rev. Med. Chem., 12 (8) 789-801.
11. Singh A. K., Lohani M., and Parthsarthy R. (**2013**) Synthesis, characterization and anti-inflammatory activity of some 1, 3, 4-oxadiazole derivatives. Iran. J. Pharm. Res., 12 (2) 319-323.
12. Singh P., Sharma P. K., Sharma J. K., Upadhyay A., and Kumar N. (**2012**) Synthesis and evaluation of substituted diphenyl-1, 3, 4-oxadiazole derivatives for central nervous system depressant activity. org. Med. Chem. Lett., 2 (1) 8-18.
13. Dawood K. M., and Gomha S. M. (**2015**) Synthesis and Anti-cancer Activity of 1, 3, 4-Thiadiazole and 1, 3-Thiazole Derivatives Having 1, 3, 4-Oxadiazole Moiety. J. Heterocycl. Chem., 52 (5) 1400-1405.
14. Chawla G., Naaz B., and Siddiqui A. A. (**2018**) Exploring 1, 3, 4-oxadiazole scaffold for anti-inflammatory and analgesic activities: a review of literature from 2005-2016. Mini-Rev. Med. Chem., 18 (3) 216-233.
15. Gan X., Hu D., Chen Z., Wang Y., and Song B. (**2017**) Synthesis and antiviral evaluation of novel 1, 3, 4-oxadiazole/thiadiazole-chalcone conjugates. Bioorg. Med. Chem. Lett., 27 (18) 4298-4301.
16. Akhtar T., Hameed S., A AL-MASOUDI N. A. J. I. M., Loddo R., and La Colla P. (**2008**) In vitro antitumor and antiviral activities of new benzothiazole and 1, 3, 4-oxadiazole-2-thione derivatives. Acta Pharm., 58 (2) 135-149.
17. Jewel P. W., and Butts J. S. (**1931**) A Method for thie Preparation of Diethyl Oxalate. J. Am. Chem. Soc., 53 (9) 3560-3561.

18. Singh A., Mohan M., and Trivedi D. R. (**2020**) Design and synthesis of malonohydrazide based colorimetric receptors for discrimination of maleate over fumarate and detection of F−, AcO− and AsO2− ions. Spectrochim. Acta A , 229 (2020) 117883-117926.
19. Yadav D., Bodke S., Biradar A., and Kenchappa R. (**2016**) Synthesis, characterization and biological evaluation of 2-(2-substituted)-5-phenyl-1, 3, 4-oxadiazole and 3, 6-diphenyl [1, 2, 4] triazole [3, 4][1, 3, 4] thiadiazole derivatives. Ind J Adv Chem Sci., 4 (3) 269-275.
20. Atif A., Ameur S., Bendaoud A., Hsissou R., Jebbari S., Ait Sir H., and Salah M. (**2025**) Comprehensive evaluation of a benzimidazole-1,3,4-oxadiazole derivative for corrosion protection of C38 steel in HCl: Experimental, molecular dynamics, monte carlo, and in silico pharmacokinetic approaches. Curr. Chem. Lett., 14 (4) 777-792
21. Farshori N. N., Rauf A., Siddiqui M. A., Al-Sheddi E. S., and Al-Oqail M. M. (**2017**) A facile one-pot synthesis of novel 2, 5-disubstituted-1, 3, 4-oxadiazoles under conventional and microwave conditions and evaluation of their in vitro antimicrobial activities. Arab. J. Chem., 10 (2) S2853-S2861.
22. Wahba A. M., Shoueir K., and Fouda A. E. A. S. (**2025**) Prediction and evaluation of pyrimidinones derivatives: DFT analysis, corrosion inhibition, and bioactivity studies. Results Surf. Interfaces., 18 (2025) 100448-100461.
23. Liu P., Xu Q., Zhang Q., Huang Y., Liu Y., Li H., Zhang R., and Lei G. (**2024**) A new insight into corrosion inhibition mechanism of the corrosion inhibitors: review on DFT and MD simulation. J Adhes Sci Tech., 38 (10) 1563-1584.
24. Obayes H. R., Al-Amiery A. A., Alwan G. H., Abdullah T. A., Kadhum A. A. H., and Mohamad A. B. (**2017**) Sulphonamides as corrosion inhibitor: experimental and DFT studies. J. Mol. Struct., 1138 (2017) 27-34.
25. Balasooriya H., Li C., and Wang F. (**2025**) Understanding Steel Corrosion: Surface Chemistry and Defects Explored Through DFT Modelling—A Review. Processes, 13 (7) 1971-2009.
26. Sundaram S., Vijayakumar V. N., and Balasubramanian V. (**2022**) Electronic and structure conformational analysis (HOMO-LUMO, MEP, NBO, ELF, LOL, AIM) of hydrogen bond binary liquid crystal mixture: DFT/TD-DFT approach. Comput. Theor. Chem., 1217 (2022) 113920.
27. Kazachenko A. S., Issaoui N., Sagaama A., Malyar Y. N., Al-Dossary O., Bousiakou L. G., Kazachenko A, S., Miroshnokova A, V., and Xiang Z. (**2022**) Hydrogen bonds interactions in biuret-water clusters: FTIR, X-ray diffraction, AIM, DFT, RDG, ELF, NLO analysis. J. King Saud Univ. Sci., 34 (8) 102350-102371.
28. Guerroudj A. R., Mughal E. U., Naeem N., Sadiq A., Al-Fahemi J. H., Asghar B. H., Boukabcha N., Chouaih A., and Ahmed S. A. (**2024**) Exploring pyrimidine-based azo dyes: vibrational spectroscopic assignments, TD-DFT investigation, chemical reactivity, HOMO-LUMO, ELF, LOL and NCI-RDG analysis. Spectrochim. Acta A., 313 (2024) 124093.
29. Reeda V. J., and Jothy V. B. (**2023**) Vibrational spectroscopic, quantum computational (DFT), reactivity (ELF, LOL and Fukui), molecular docking studies and molecular dynamic simulation on (6-methoxy-2-oxo-2H-chromen-4-yl) methyl morpholine-4-carbodithioate. J. Mol. Liq., 371 (2023) 121147.
30. Sarau H. M., Foley J., Moonsammy G., and Wiebelhaus V. D. (**1975**) Metabolism of dog gastric mucosa. Nucleotide levels in parietal cells. J. Biol. Chem., 250 (21) 8321-8329.
31. Al-Qurashi O. S., and Wazzan N. (**2022**) Molecular and periodic DFT calculations of the corrosion protection of Fe (1 1 0) by individual components of Aerva lanata flower as a green corrosion inhibitor. J. Saudi Chem. Soc., 26 (6) 101566-101575.
32. Badr E. A., Bedair M. A., and Shaban S. M. (**2018**) Adsorption and performance assessment of some imine derivatives as mild steel corrosion inhibitors in 1.0 M HCl solution by chemical, electrochemical and computational methods. Mater. Chem. Phys., 219 (2018) 444-460.
33. Puthanveedu V., and Muraleedharan K. (**2023**) Study on structural detailing of gossypetin and its medicinal application in UV filtering, radical scavenging, and metal chelation open up through NCI, TD-DFT, QTAIM, ELF, and LOL analysis. Comput. Theor. Chem., 1225 (2023) 114126.
34. Lashgari S. M., Bahlakeh G., and Ramezanzadeh B. (**2021**) Detailed theoretical DFT computation/molecular simulation and electrochemical explorations of Thymus vulgaris leave extract for effective mild-steel corrosion retardation in HCl solution. J. Mol. Liq., 335 (5) 115897-115913.
35. Archer D. W. (**1975**) Criminal exposure of physician assistants. J. Leg. Med., 3 (10) 32-34.
36. Shibaeva A. N. (**1975**) The organization of health education meetings, verbal reports, carnivals, reader's conferences. Fel'dsher i akusherka, 40 (9) 31-34.
37. Damej M., Molhi A., Lgaz H., Hsissou R., Aslam J., Benmessaoud M., Rezki N., Lee H, S., and Lee D. E. (**2023**) Performance and interaction mechanism of a new highly efficient benzimidazole-based epoxy resin for corrosion inhibition of carbon steel in HCl: A study based on experimental and first-principles DFTB simulations. J. Mol. Struct., 1273 (2023) 134232.

© 2026 by the authors; licensee Growing Science, Canada. This is an open access article distributed under the terms and conditions of the Creative Commons Attribution (CC-BY) license (http://creativecommons.org/licenses/by/4.0/).